Title
Diffractive optical elements based on Fourier optical techniques: A new class of optics for extreme ultraviolet and soft x-ray wavelengths

Journal
Applied Optics, 41(35)

Author
Attwood, David

Publication Date
2002-05-05

Diffractive optical elements based on Fourier optical techniques: A new class of optics for extreme ultraviolet and soft x-ray wavelengths

Chang Chang[1,2], Patrick Naulleau[1], Erik Anderson[1], Kristine Rosfjord[1,2], David Attwood[1,2]

[1]Center for X-Ray Optics,
Lawrence Berkeley National Laboratory, Berkeley, CA 94720

[2]Department of Electrical Engineering & Computer Sciences,
University of California, Berkeley, CA 94720

cnchang@lbl.gov

A diffractive optical element, based on Fourier optics techniques, for use in extreme ultraviolet/soft x-ray experiments has been fabricated and demonstrated. This diffractive optical element, when illuminated by a uniform plane wave, will produce two symmetric off-axis first order foci suitable for interferometric experiments. The efficiency of this optical element and its use in direct interferometric determination of optical constants are also discussed. Its use opens a new era in the use of sophisticated optical techniques at short wavelengths.

OCIS codes: 999.9999, 000.0000 Fill in OCIS codes here.

1. Introduction

Coherent extreme ultraviolet (EUV) and soft x-ray (SXR) radiation[4] facilitates phase-sensitive techniques that provide new opportunities in various fields, e.g. biological imaging, material characterization, and nanotechnology. However, challenges are presented in that very limited optical elements are available at these wavelengths. No appropriate materials exist for lenses and prisms due to high absorption. Most experiments either utilize low efficiency diffractive optics such as Fresnel zoneplates, or glancing incidence reflection mirrors and normal incidence multi-layer mirrors which result in restrictive off-axis optical systems and limited spectral region, respectively. Therefore, devising novel optical elements that can effectively and efficiently achieve wavefront shaping is of crucial importance for researches conducted at EUV/SXR wavelengths. Here, Fourier optical techniques are introduced to accomplish the desired wavefront manipulation.

In our first example of these new techniques, we have designed and fabricated, based on Fourier optics techniques, a diffractive optical element which combines the functions of the grating and zoneplate through a bit-wise XOR operation. Using this compound diffractive optical element allows the efficiency and the contrast of the interferometer to be greatly increased. This optical element has been used in an EUV interferometer to directly determine the index of refraction at EUV wavelengths. Similar activities are underway at soft x-ray wavelengths.

2. XOR pattern

This XOR diffractive optical element is obtained by combining a 50% duty-cycle binary intensity grating and a 50% duty-cycle intensity zoneplate. The binary grating and zoneplate are first pixelized, with each pixel being either 1 or 0 for transmission and absorption, respectively. The two pixelized patterns are then overlapped and compared pixel by pixel to produce the resulting XOR pattern, i.e. at each pixel position, if the pixel values of the grating and zoneplate are the same

(both 0's or both 1's), the value of the corresponding pixel on the XOR pattern is 0. Otherwise, the value of the corresponding pixel on the XOR pattern is 1.

For a 50% duty-cycle grating of period d, the transmitted intensity function is

$$G(x,y) = \frac{1}{2}\left[1 + sgn\left(\cos \nu x\right)\right] \tag{1}$$

where $\nu = 2\pi/d$.

Similarly, for a 50% duty-cycle zoneplate of diameter D and outermost zone-width Δr, the transmitted intensity function is[1]

$$ZP(x,y) = \frac{1}{2}\left[1 + sgn\left(\cos \gamma\, r^2\right)\right] \tag{2}$$

where $r = \sqrt{x^2 + y^2}$ and $\gamma = \frac{\pi}{\Delta r(D - \Delta r)}$.

Expand these two patterns in their Fourier series,

$$G(x,y) = \sum_{m=-\infty}^{\infty} \frac{\sin(m\pi/2)}{m\pi}\, e^{-jm\nu x} \tag{3}$$

and

$$ZP(x,y) = \sum_{n=-\infty}^{\infty} \frac{\sin(n\pi/2)}{n\pi}\, e^{-jn\gamma\, r^2}. \tag{4}$$

Note that by comparing the Fourier series of a zoneplate to a lens, one finds that the zoneplate can be regarded as a series of lenses with n^{th} order focal length $f_n = \frac{-\pi}{n\lambda\gamma}$.

The XOR pattern of the combined grating and the zoneplate is obtained by forming

$$
\begin{aligned}
XOR(x,y) &= G(x,y) + ZP(x,y) - 2G(x,y)ZP(x,y) \\
&= \sum_{m=-\infty}^{\infty} \frac{\sin(m\pi/2)}{m\pi}\, e^{-jm\nu x} + \sum_{n=-\infty}^{\infty} \frac{\sin(n\pi/2)}{n\pi}\, e^{-jn\gamma\, r^2} \\
&\quad - 2\left[\frac{1}{2} + \sum_{\substack{m=-\infty \\ m\neq 0}}^{\infty} \frac{\sin(m\pi/2)}{m\pi}\, e^{-jm\nu x}\right]\left[\frac{1}{2} + \sum_{\substack{n=-\infty \\ n\neq 0}}^{\infty} \frac{\sin(n\pi/2)}{n\pi}\, e^{-jn\gamma\, r^2}\right] \qquad (5) \\
&= \frac{1}{2} - 2\left[\sum_{\substack{m=-\infty \\ m\neq 0}}^{\infty} \frac{\sin(m\pi/2)}{m\pi}\, e^{-jm\nu x}\right]\left[\sum_{\substack{n=-\infty \\ n\neq 0}}^{\infty} \frac{\sin(n\pi/2)}{n\pi}\, e^{-jn\gamma\, r^2}\right].
\end{aligned}
$$

This combined diffractive element, when illuminated by a uniform wavefront, has the interesting property that it produces two symmetric off-axis focal spots, $(m,n) = (\pm 1, 1)$, at the back focal plane of the zoneplate. Note that both the grating and the zoneplate have to be of 50% duty-cycle for the on-axis focal spot to disappear, i.e. $m \neq 0$ and $n \neq 0$ in the summation. The separation of these two beam spots Δx can be determined by multiplying the two exponentials in Eq.(5), completing the square for x-terms, thus resulting in $\Delta x = 2\Delta r(D - \Delta r)/d \approx 2\Delta r D/d$. Note that this separation is independent of wavelength λ. Thus as the wavelength is varied for spectral determinations of δ and β, the focal length (distance from the XOR pattern to the sample mask) varies, but the lateral separation of the two beam spots remains fixed. The invariance of the spot separation over wavelength allows the EUV interferometer to operate at different wavelengths without the need of changing the image-plane sample mask. This is a desirable property for EUV interferometers since the scale of the sample mask for EUV applications requires it to be micro/nano-fabricated, thus immutable after being made.

A. Simulation of the XOR pattern

A computer simulation is performed to see if these patterns produce the expected results. An XOR pattern of a grating (period $d = 16\mu m$) and a zoneplate (outermost zone-width $\Delta r = 0.2\mu m$,

diameter $D = 400\mu m$) is produced, as shown in Fig. 1(a). This pattern is then Fresnel-propagated to the first order focal plane of the zoneplate and the resulting intensity distribution is shown in Fig. 1(b). As expected, only two off-axis spots exist in this focal plane.

3. Efficiency of the XOR pattern

The XOR pattern, as expressed in Eq. 5, gives the efficiencies of the individual orders.

First of all, we need to determine the overall transparent area of this XOR pattern. Since we know that the percent of transparent area on the grating and the zoneplate is 1/2, we find that the overall transparent area of the XOR pattern to be $1/2 + 1/2 - 2(1/2)(1/2) = 1/2$ from Eq. 5.

Next, we calculate the efficiency of individual orders from their relative strength. From Eq. 5, we have, for $m, n \neq 0$,

$$\eta_{m,n} = \begin{cases} \dfrac{2^2(1/m\pi)^2(1/n\pi)^2}{(1/2)^2 + 2^2(2\frac{1}{8})(2\frac{1}{8})} \times \dfrac{1}{2} = \dfrac{4}{m^2n^2\pi^4} & \text{if } m, n \text{ are both odd,} \\ \\ 0 & \text{if } m \text{ or } n \text{ is even.} \end{cases} \tag{6}$$

where $\sum_{k=0}^{\infty} \frac{1}{(2k+1)^2} = \frac{\pi^2}{8}$ is used in the calculation.

Another way to look at this is that we can think of this XOR pattern as a binary amplitude zoneplate, multiplied by a π-phase-shift grating which does not have any absorption. Therefore, the overall absorption of this XOR pattern is the same as that of a binary amplitude zoneplate, i.e. 1/2 and the efficiency of its individual orders is given by multiplying the corresponding orders of the binary amplitude zoneplate and the π-phase-shift grating. The efficiency η_m of a 50% duty-cycle π-phase-shift grating is

$$\eta_m = \begin{cases} \dfrac{4}{m^2\pi^2} & \text{for } m = \pm 1, \pm 3, \cdots, \\ \\ 0 & \text{for } m \text{ is even.} \end{cases} \tag{7}$$

And the efficiency η_n of a binary amplitude zoneplate is

$$\eta_n = \begin{cases} \dfrac{1}{n^2\pi^2} & \text{for } n = \pm 1, \pm 3, \cdots, \\ 0 & \text{for } n \text{ is even.} \end{cases} \tag{8}$$

By comparing Eq. 6 with Eq. 7 and Eq. 8, we indeed see that the efficiency of the individual orders of the XOR pattern, $\eta_{m,n}$, is given by $\eta_m \times \eta_n$, , i.e. the multiplication of the corresponding orders of the phase grating and amplitude zoneplate.

4. Visible light experiment

A first XOR pattern, designed for proof-of-principle testing at visible wavelengths, is fabricated using e-beam lithography[5] in order to directly observe the intensity distribution at the back focal plane. The grating used in this visible version has a period of $5\mu m$,the zoneplate diameter is $5mm$ and the outermost zone-width is $2\mu m$. A screen is put at its back plane, which is $15.8mm$ away from this visible XOR pattern. A collimated He-Ne laser beam ($\lambda = 633\, nm$) is then used to illuminate this visible version XOR pattern and the resulting intensity distribution at the back focal plane is shown in Fig. 2(a). As expected, the two symmetric off-axis foci are directly observable and there is no on-axis focus presented. The separation between these two off-axis spots are measured to be $4mm$, which agrees with the designed value. As a comparison, an "OR" pattern made from the same grating and zoneplate is also fabricated and tested. The effect of combining the grating and zoneplate through an bit-wise OR operation is equivalent to that of placing them in tandem. Therefore, this OR pattern demonstrates the back focal plane intensity distribution of a traditional separate grating and zoneplate setup. Fig. 2(b) shows the resulting intensity distribution at the back focal plane of this OR pattern. Three foci are clearly observed, with the strongest focus on-axis and two weaker symmetric off-axis foci. The separation between the on-axis and the off-axis spots are measured to be $2mm$, which again agrees with the designed value.

5. First use in EUV interferometry

The XOR pattern employed in our first application to EUV interferometry is fabricated using the same e-beam lithography tool and an SEM image of the actual pattern is shown in Fig. 3. The period d of the grating used here is $16\mu m$ ($8\mu m$ pitch) and the zoneplate has a diameter $D = 400\mu m$ and a outermost zone-width $\Delta r = 0.2\mu m$. Undulator beamline 12 at the Advanced Light Source provides the EUV radiation for this measurement.[4] The wavelength at which this measurement was performed is $\lambda = 16.53\, nm$ (75 eV) and the monochromator at the beamline is set at $\lambda/\Delta\lambda = 1100$.

This interferometer utilizes the strongest non-zeroth order, i.e. $(m, n) = (\pm 1, 1)$, which has a theoretical efficiency of $4/\pi^2 \times 1/\pi^2 = 4/\pi^4 \sim 4.1\%$ as given by Eq. 6. Experimentally, the efficiency of this XOR pattern is measured by recording the total counts on the CCD while scanning a knife-like beam-stop transversely across the back focal plane. Starting with the beam-stop placed at the back focal plane such that the entire beam is blocked, as the beam-stop slowly moves aside, the total counts on the CCD increases, allowing fractions of light to pass. The result of this efficiency measurement is shown in Fig. 4. The two abrupt steps at the center is caused by the two symmetric off-axis first order foci, $(m, n) = (\pm 1, 1)$, being released one at a time by the scanning beam-stop. However, when determining the efficiency of the $(m, n) = (\pm 1, 1)$ order, the effect of straight through light needs to be removed. Since the position of the transversely scanning beam-stop is directly proportional to the fraction of the straight through light that passes it, the effect of straight through light can be determined by the constant slope of the two straight sections. After removing the effect of the straight through light by least-square fitting the slope of the two straight sections, the individual strength of the $(m, n) = (\pm 1, 1)$ order is shown to be around 4.0%, which agrees with the theoretical value.

Comparing with the traditional separate binary grating and zoneplate setup, in which the $\pm 1st$ orders of the grating are being focused by the first order of the zone-plate with a overall efficiency of

$1/\pi^4 \sim 1.0\%$, this XOR pattern provides a 4 times improvement in theory. In practice, the required exposure time actually reduces about 10 times due to the fact that the substrates on which these optical elements are fabricated have finite absorption and only one substrate is needed in this case. This improvement in efficiency enables the first direct measurement of refractive index at EUV wavelengths.[6]

6. A next step: computer generated hologram for EUV/SXR region

The design concept is depicted in Fig. 5(a). In a computer simulation, the object wave (in red) which consists of two converging spherical wavefronts is encoded by a reference plane wave (in blue) to form an interference pattern (hologram), as shown in Fig. 5(b). This computer generated hologram (CGH), when illuminated by the reference plane wave, will produce two converging spherical wavefronts which can be used for interferometric experiments. Note the these two spherical wavefronts are identical and symmetrically distributed with respect to the optical axis. Comparing with a typical grating-zoneplate setup, where the zeroth order of the grating is centered on axis at the zoneplate's first order focal plane, the wavefront produced by this computer generated hologram indeed has better flux throughput and is more suitable for interferometry due to its symmetricalness.

To nano-fabricate this CGH, it is necessary to binarize the "smooth" areal interference pattern (Fig. 5(b)) into 0's and 1's. This binarized pattern, shown in Fig. 5(c), will then be used to produced the CAD file that nano-fabricates the holographic optical element. To see the effect of binarization on the re-constructed wavefront, this binarized holographic optical element is Fresnel-propagated to the plane where the object wave converges to two points and the intensity distribution is shown in Fig. 5(d). No significant higher order effects are observed.

7. Conclusion

This paper demonstrates for the first time a novel diffractive optical element based on Fourier optics techniques. It is shown, both in theory and in experiment, that by combining two diffractive elements, a grating and a zoneplate, through a bit-wise XOR operation, the resultant optical element produced a new functionality, two symmetric off-axis foci with a higher efficiency. The two symmetric off-axis foci at the back focal plane are used in an EUV experiment to directly measure both the real and imaginary parts of the refractive index. Specifically, it is shown that interferometric experiments that require better contrast and higher coherent power benefit from this XOR design, due to the symmetricalness of the intensity distribution at the back focal plane and the improved overall efficiency, respectively. This group of optical elements shown in this paper brings sophisticated Fourier optical techniques to open new experimental frontiers in an area rich with opportunities on nanometer scales and with element-specific identifications and applications.

8. Acknowledgement

The authors would like to thank Bruce Harteneck for help with SEM, and Phil Batson's great engineering team: Brian Hoef, Paul Denham, Seno Rekawa, for excellent engineering support. This work was supported by the Director, Office of Science, Office of Basic Energy Sciences, Division of Materials Sciences and Engineering, of the U.S. Department of Energy under Contract No. DE-AC03-76SF00098.

References

1. J.W. Goodman, *Introduction to Fourier optics*, 2nd ed., (McGraw-Hill, New York, 1996).

2. M. Born, and E. Wolf, *Principles of optics: electromagnetic theory of propagation, interference and diffraction of light*, 6th ed., Cambridge University Press, 1997).

3. D. T. Attwood, *Soft x-rays and extreme ultraviolet radiation : principles and applications*, (Cambridge University Press, 1999).

4. D.T. Attwood, P. Naulleau, K.A. Goldberg, E. Tejnil, C. Chang, R. Beguiristain, P. Batson, J. Bokor, E.M. Gullikson, M. Koike, H. Medecki, J.H. Underwood, "Tunable coherent radiation in the soft X-ray and extreme ultraviolet spectral regions", *IEEE J. Quantum Electron.*, **35**, 709-20 (1999).

5. E.H. Anderson, D.L. Olynick, B. Harteneck, E. Veklerov, G. Denbeaux, W. Chao, A. Lucero, L. Johnson, D. Attwood, "Nanofabrication and diffractive optics for high-resolution X-ray applications", *J. Vac. Sci. Technol. B*, **18**, 2970-5 (2000).

6. C. Chang, P. Naulleau, E.H. Anderson, E.M. Gullikson, K.A. Goldberg, D. Attwood, "Direct index of refraction measurement at extreme ultraviolet wavelength region with a novel interferometer", *Opti. Lett.*, accepted for publication.

List of Figures

Figure 1:

Computer simulation of the XOR pattern: The parameters used in this simulation is equal to the actual fabricated element. The pattern in (a) is obtained by taking the "exclusive or (XOR)" of the binary grating and zone-plate. 4096×4096 pixels are used to generated this pattern. Note that pixelization of this fine pattern gives rise to Moiré fringes in (a). An enlarged center part of the XOR pattern is also shown in (a), for a demonstration of the Moiré effect and comparison with Fig. 3. This pattern is then Fresnel-propagated in computer by one focal length and the resulting intensity distribution is shown in (b). The two symmetric off-axis first order foci is clearly visible in this simulation. The other two outer spots are caused by the second order ($m = \pm 2$) of the grating, with 4 times lower intensity.

Figure 2:

A visible experiment is performed in order to directly verify the intensity distribution at the back focal plane of the XOR pattern. For comparison, an OR pattern obtained by taking the bit-wise OR of a grating and a zoneplate is also fabricated. The effect of this OR pattern is equivalent to that of a grating and a zoneplate placed in tandem, which is the conventional setup for interferometric experiments. Part (a) shows that the intensity distribution at the back focal plane of the XOR pattern consists of only two symmetric off-axis foci, as predicted by the theory. As a comparison, the focal plane intensity distribution of the OR pattern is shown in (b), which has three foci, with one strongest on-axis focus and two weaker off-axis symmetric foci. The grating used by the XOR and OR patterns in this visible experiment has a period of $5\,\mu m$ and the diameter and the outermost zone-width of the zoneplate is $D = 5\,mm$ and $2\,\mu m$, respectively. A He-Ne laser ($\lambda = 633\,nm$) is used for illuminating the XOR and OR patterns.

Figure 3:

The center part of the XOR pattern is shown. This diffractive optical element is obtained by taking the bit-wise XOR of a binary amplitude grating and a binary amplitude zoneplate. The functionality of this XOR pattern is equivalent to that of a binary phase grating overlapping a binary amplitude zoneplate, as discussed in the text. The grating used here has a $16\mu m$ period ($8\mu m$ pitch) and the zoneplate has a $400\mu m$ diameter and a $0.2\mu m$ outermost zone-width.

Figure 4:

The efficiency of this XOR pattern is measured by scanning a knife-like beam-stop across the focal plane. Starting with the beam-stop placed at the back focal plane such that the entire beam is blocked, as the beam-stop slowly moves aside, the total counts on the CCD increases, allowing fractions of light to pass. The constant slope of the two straight sections results from the effect of zeroth order (straight through) light. The two abrupt steps at the center is caused by the two symmetric off-axis first order foci being released one at a time by the beam-stop. Their strength is shown to be around 4.0%, which agrees with the theoretical value.

Figure 5:

In part (a), the object wave (in red) which consists of two converging spherical wavefronts interferes with a reference plane wave (in blue) and the resulting intensity interference pattern, which is usually referred to as Computer Generated Hologram, is shown in (b). This CGH is then binarized for nanofabrication by e-beam lithography. Part (c) shows its binarized from. When illuminated by a uniform plane wave, this optical element reconstructs the object wave (two converging spherical waves) as shown in (d). Note that the two spots are symmetrically off-axis.

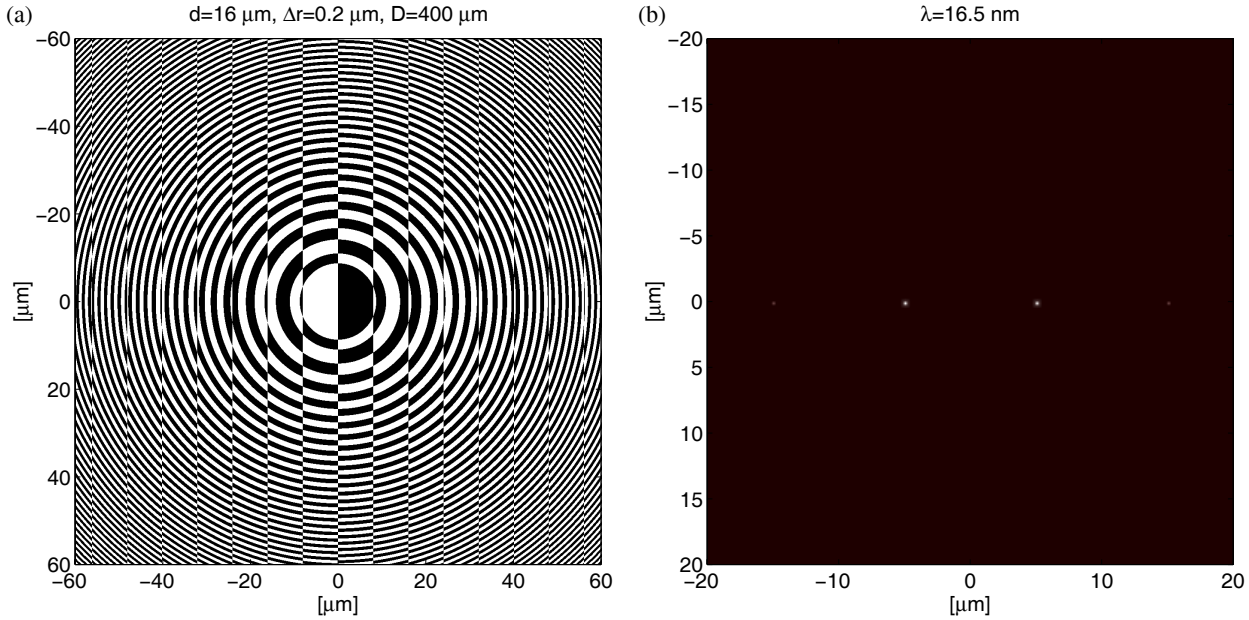

Fig. 1. Computer simulation of the XOR pattern: The parameters used in this simulation is equal to the actual fabricated element. The pattern in (a) is obtained by taking the "exclusive or (XOR)" of the binary grating and zone-plate. 4096×4096 pixels are used to generated this pattern. Note that pixelization of this fine pattern gives rise to Moiré fringes in (a). An enlarged center part of the XOR pattern is also shown in (a), for a demonstration of the Moiré effect and comparison with Fig. 3. This pattern is then Fresnel-propagated in computer by one focal length and the resulting intensity distribution is shown in (b). The two symmetric off-axis first order foci is clearly visible in this simulation. The other two outer spots are caused by the second order ($m = \pm 2$) of the grating, with 4 times lower intensity.

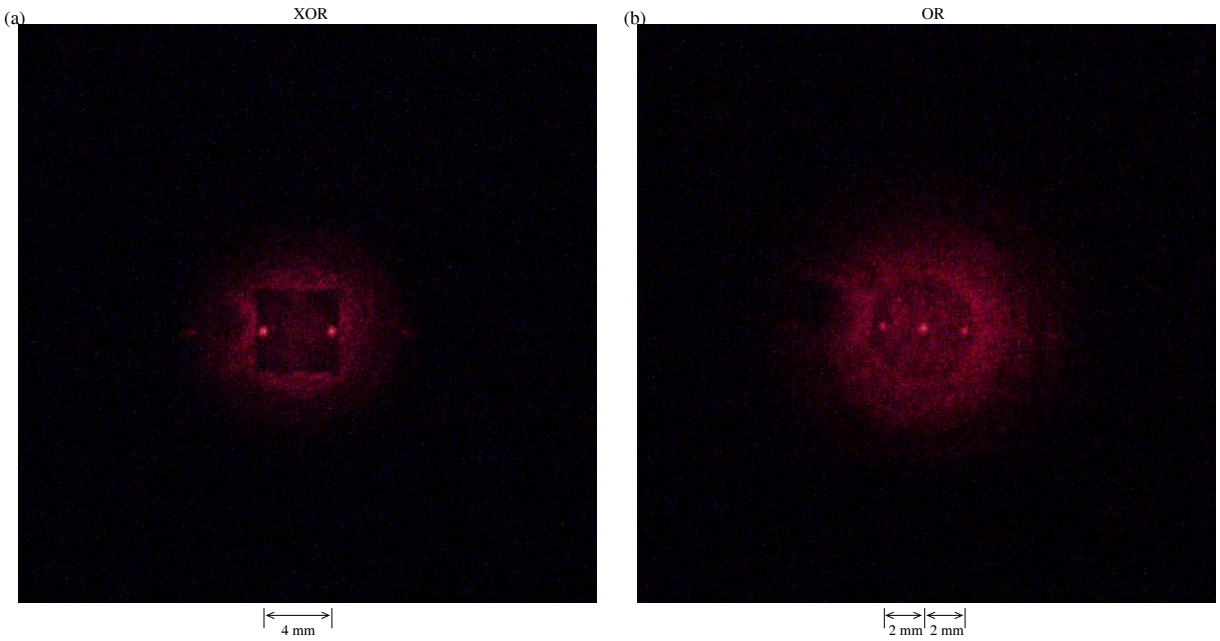

Fig. 2. A visible experiment is performed in order to directly verify the intensity distribution at the back focal plane of the XOR pattern. For comparison, an OR pattern obtained by taking the bit-wise OR of a grating and a zoneplate is also fabricated. The effect of this OR pattern is equivalent to that of a grating and a zoneplate placed in tandem, which is the conventional setup for interferometric experiments. Part (a) shows that the intensity distribution at the back focal plane of the XOR pattern consists of only two symmetric off-axis foci, as predicted by the theory. As a comparison, the focal plane intensity distribution of the OR pattern is shown in (b), which has three foci, with one strongest on-axis focus and two weaker off-axis symmetric foci. The grating used by the XOR and OR patterns in this visible experiment has a period of $5\,\mu m$ and the diameter and the outermost zone-width of the zoneplate is $D = 5\,mm$ and $2\,\mu m$, respectively. A He-Ne laser ($\lambda = 633\,nm$) is used for illuminating the XOR and OR patterns.

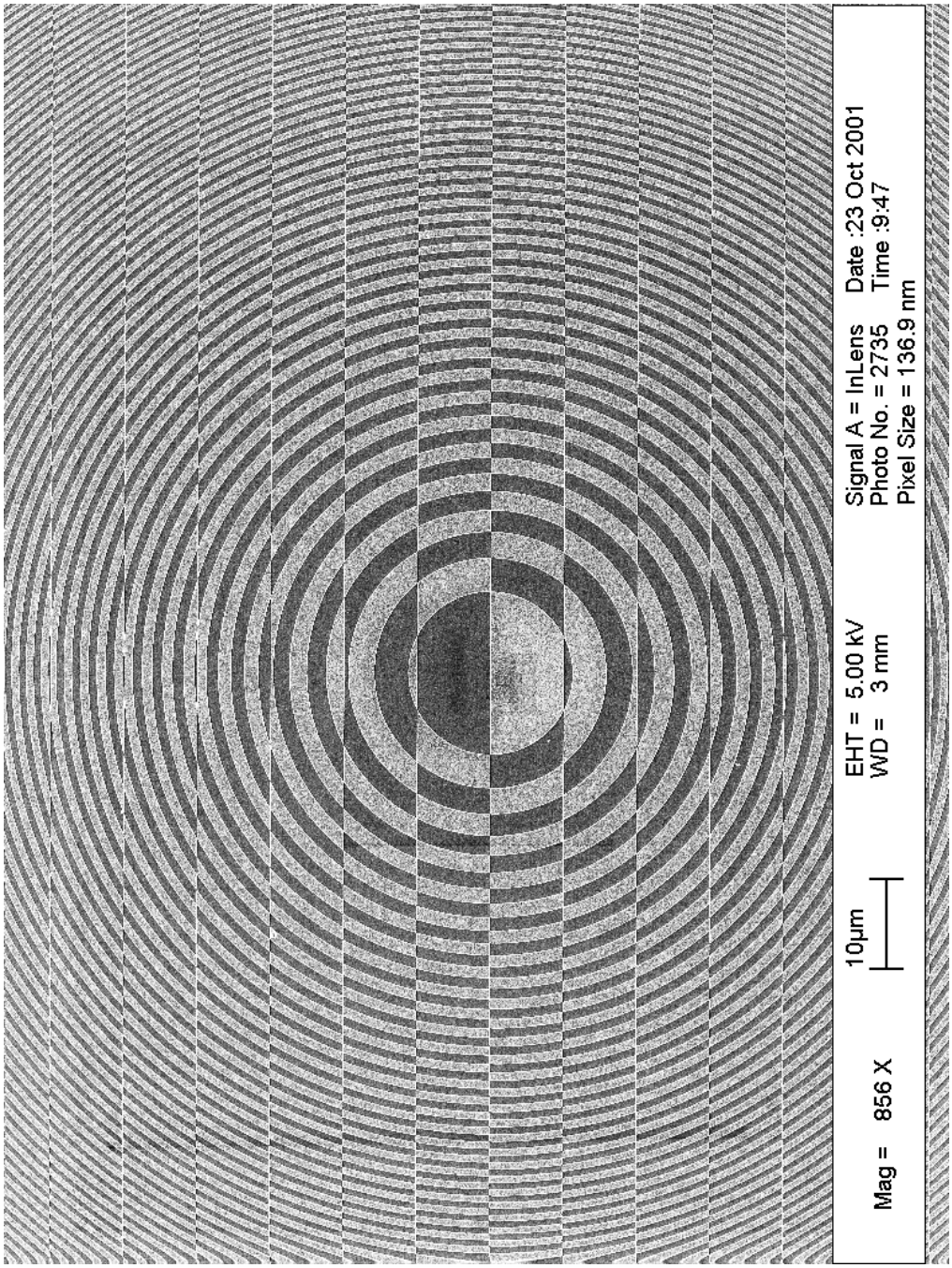

Fig. 3. The center part of the XOR pattern is shown. This diffractive optical element is obtained by taking the bit-wise XOR of a binary amplitude grating and a binary amplitude zoneplate. The functionality of this XOR pattern is equivalent to that of a binary phase grating overlapping a binary amplitude zoneplate, as discussed in the text. The grating used here has a $16\mu m$ period ($8\mu m$ pitch) and the zoneplate has a $400\mu m$ diameter and a $0.2\mu m$ outermost zone-width.

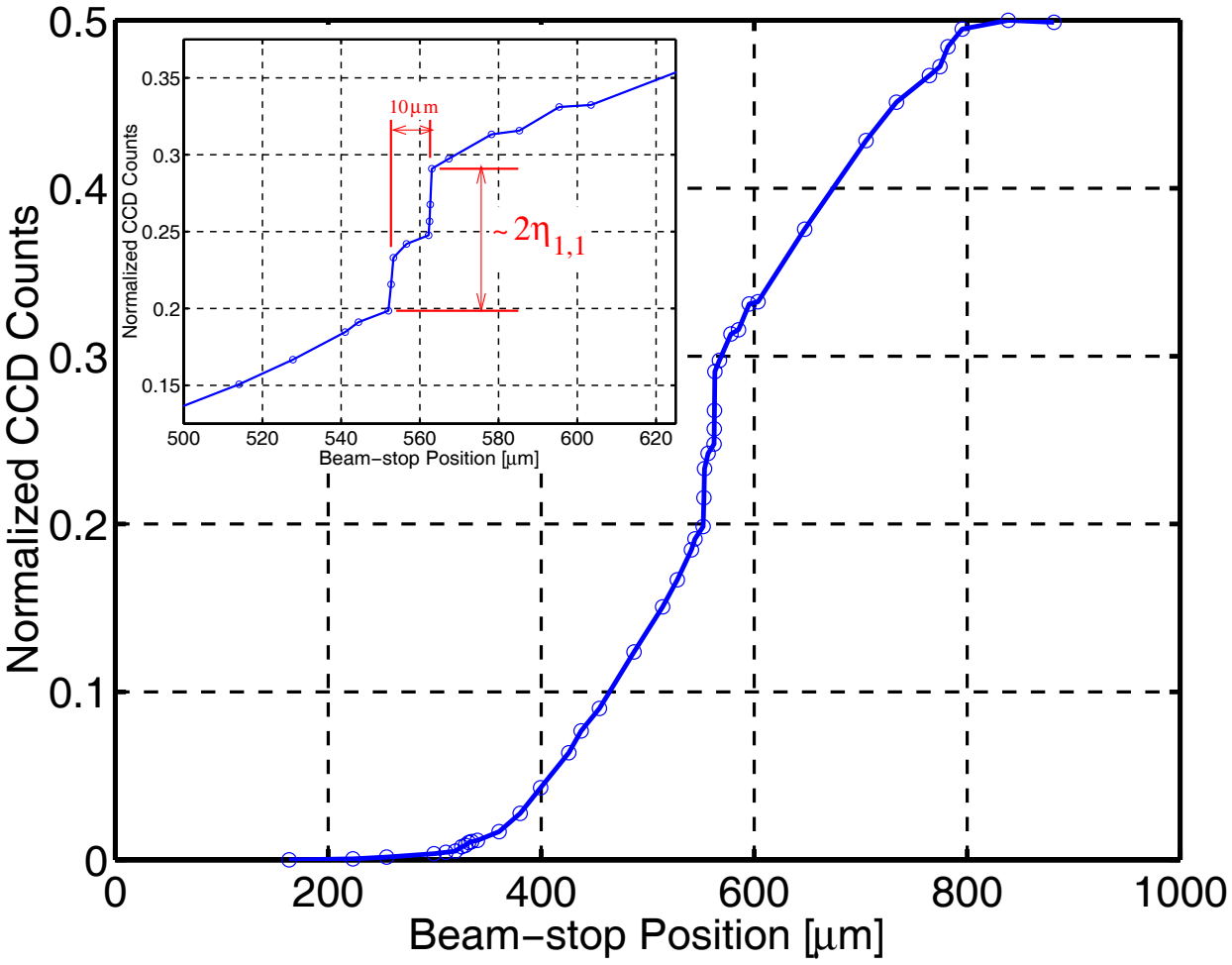

Fig. 4. The efficiency of this XOR pattern is measured by scanning a knife-like beam-stop across the focal plane. Starting with the beam-stop placed at the back focal plane such that the entire beam is blocked, as the beam-stop slowly moves aside, the total counts on the CCD increases, allowing fractions of light to pass. The constant slope of the two straight sections results from the effect of zeroth order (straight through) light. The two abrupt steps at the center is caused by the two symmetric off-axis first order foci being released one at a time by the beam-stop. Their strength is shown to be around 4.0%, which agrees with the theoretical value.

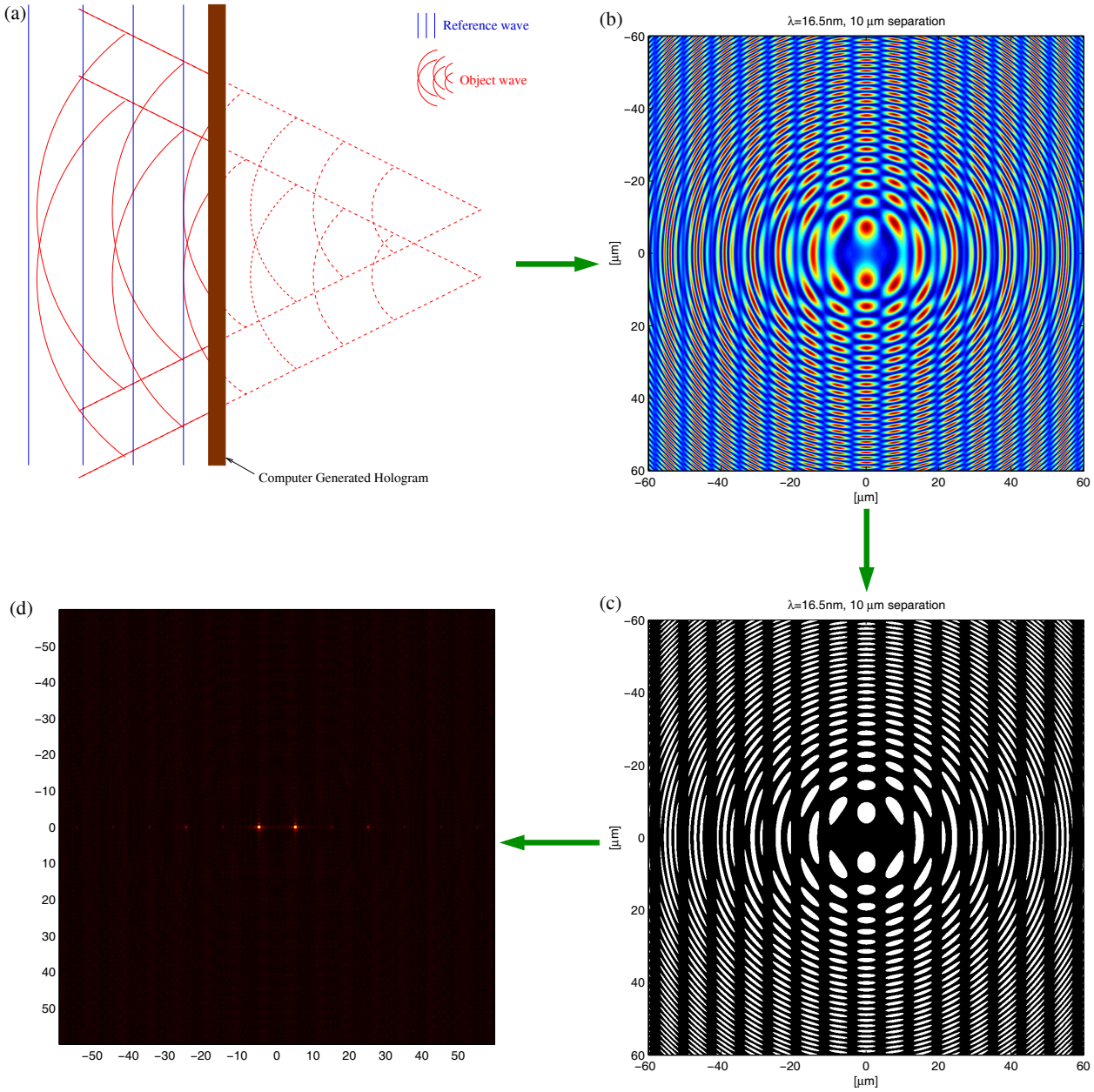

Fig. 5. In part (a), the object wave (in red) which consists of two converging spherical wavefronts interferes with a reference plane wave (in blue) and the resulting intensity interference pattern, which is usually referred to as Computer Generated Hologram, is shown in (b). This CGH is then binarized for nanofabrication by e-beam lithography. Part (c) shows its binarized from. When illuminated by a uniform plane wave, this optical element reconstructs the object wave (two converging spherical waves) as shown in (d). Note that the two spots are symmetrically off-axis.